

# Tangential Effects on Magnetic Vibrations and Acoustic Noise of Induction Machines using Subdomain Method and Electromagnetic Vibration Synthesis

Emile Devillers<sup>1,2</sup>, Michel Hecquet<sup>1</sup>, Jean Le Besnerais<sup>2</sup>, Margaux Régniez<sup>2</sup>

<sup>1</sup>L2EP; Université de Lille 1, Ecole Centrale de Lille, Villeneuve d'Ascq, France, emile.devillers@phd.centralelille.fr

<sup>2</sup>EOMYS ENGINEERING; Lille-Hellemmes, France, contact@eomys.com

**Abstract**— In the vibroacoustic analysis of electrical machines, the effect of the tangential magnetic force on the vibrations is generally neglected compared with the radial magnetic force, as well as the effect of the tangential flux density on the radial force, especially for induction machines. In this paper, these two assumptions are studied for the case of an induction machine at no-load and load states. First, time and space distribution of the magnetic flux density – including radial and tangential components – is computed in the air gap using a new semi-analytical subdomain modeling technique of squirrel-cage induction machine, including all harmonics. Then, magnetic forces are obtained by applying the Maxwell stress tensor. Stator vibrations are finally computed with and without neglecting the tangential effects using electromagnetic vibration synthesis implemented in MANATEE software. Results show that both tangential effects have a small impact on the maximum emitted noise in the case of the studied induction machine.

**Keywords**— Noise and vibrations, Magnetic flux density, Analytical model, Electrical machines, Electromagnetic forces.

## I. INTRODUCTION

In electrical machines, the study of noise and vibrations due to Maxwell magnetic forces first requires the knowledge of the time and space distribution of the air gap magnetic flux density. Indeed, it is well known that a very small harmonic in the magnetic forces can induce large acoustic noise and vibrations due to a resonance with a structural mode of the machine. Besides, radial and tangential components of the magnetic forces depends on the radial and tangential components of the flux density. Hence both components of the air gap magnetic flux density have to be determined in time and space domains for an accurate prediction of magnetic forces. Due to the quadratic relationship between Maxwell forces and flux density, flux density waves with high number of pole pairs can generate magnetic force waves with low number of pole pairs, which are the most harmful in terms of vibrations as the structure is less stiff. The accuracy of the calculation of the flux density must therefore include high order spatial harmonics.

The flux density can be accurately computed using numerical methods such as Finite Element Method (FEM).

However, they are very time-consuming when setting a fine discretization to observe high time and space harmonics of flux density, as well as a fine speed discretization to observe resonances occurring at variable speed as shown in [1]. In conclusion, numerical methods are not suitable to the fast analysis of noise and vibrations due to magnetic forces in the early electromagnetic design iteration loops. The time and space distribution of the air gap flux density can be computed much faster using the permeance/mmf (magnetomotive force) analytical method which is used in many vibroacoustic studies of induction machines [1]. Though, permeance/mmf only gives insight on the radial component of the magnetic flux density.

If the tangential flux density is unknown, two assumptions are necessary made. First, the effect of tangential flux density on radial force is neglected [2]. This assumption is also found in the analysis of permanent magnet synchronous machines (PMSM) [3]. However, it may introduce an error on forces computation especially for machines with large airgap, such as permanent magnet generators for wind turbine applications [4]. Secondly, the effect of tangential force on radial vibrations is neglected because the tangential force is unknown. If the external structure is equivalent to a thin cylinder, tangential forces may not generate radial vibrations as in [5] in case of PMDC machine with external rotor. In case of a machine with external slotted stator, this assumption still need to be validated, especially when there is an interaction between tangential forces and tooth bending modes which may induce radial deflections of the stator yoke in addition with those due to radial forces [6][7].

Furthermore, radial and tangential components of the flux density can be accurately computed by the recently developed SubDomain Method (SDM), which is accurate and usually faster than FEM [8]. The method has already been used for magnetic forces computation [9] and fast vibroacoustic studies of PMSM [10]. SDM has also been extended to Squirrel Cage Induction Machines (SCIM) even if there are fewer references [11][12][13]. Both models developed in [11] and [12] are dedicated to compute global performances such as mean torque but may not account for all the harmonic content required for noise and vibrations analysis. In [13], the subdomain model is coupled with a harmonic Equivalent Electric Circuit and gives

accurate results regarding torque ripple and harmonics of induced rotor currents. However, it has never been used for vibroacoustic analysis though it could be suitable to compute other magnetic forces. For this purpose, a new subdomain model of SCIM has been developed, based on [11][12], and especially dedicated to fast vibroacoustic simulations. The model includes the effect of stator and rotor slotting harmonics and the effect of the phase-belt harmonics (space harmonics of the stator magnetomotive force) on the eddy-currents induced in the rotor bars.

In this paper, radial and tangential flux densities are computed using the new SDM at no-load and load states. Then, magnetic forces are deduced using Maxwell stress tensor. Stator vibrations are finally computed with an Electromagnetic Vibration Synthesis (EVS) using the coupling between MANATEE simulation environment [14] and Optistruct. The EVS is performed with and without both tangential effects to study their impact on the vibrations on a specific induction machine.

## II. MACHINE DESCRIPTION

The studied machine is the squirrel cage induction machine dedicated to railway traction. Its properties are listed in TABLE I. The stator winding is a three-phased double layer distributed winding with a shorted pitch ratio of 5/6 as shown on Fig. 1.

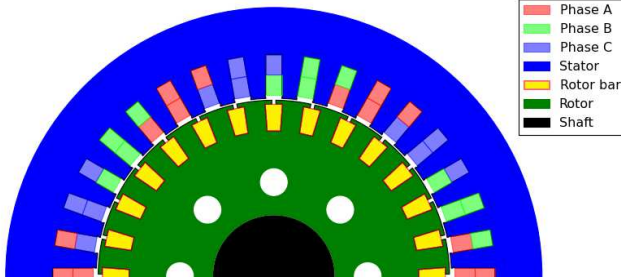


Fig. 1 Cross sectional view of the SCIM

TABLE I. LIST OF GEOMETRICAL PARAMETERS

Machine parameters	Symbol	Value
Nominal supply frequency	$f_s$	60 [Hz]
Stator phase current at no-load	$I_{nl}$	60 [A]
Stator phase current at load	$I_{load}$	120 [A]
Number of rotor bars	$Z_r$	28
Number of stator slots	$Z_s$	36
Number of pole pairs	$p$	3
Rotor bars inner radius	$R_1$	108 [mm]
Rotor slot opening inner radius	$R_2$	128 [mm]
Airgap inner radius	$R_3$	131 [mm]
Airgap outer radius	$R_4$	135.5 [mm]
Stator slots outer radius	$R_5$	165 [mm]
Rotor bars angular width	$\alpha$	0.1016 [rad]
Rotor slots opening angular width	$\beta$	0.0229 [rad]
Stator slots angular width	$\gamma$	0.0906 [rad]
Rotor bar electrical conductivity	$\sigma$	$5.78e7$ [S]

## III. ELECTROMAGNETIC MODEL

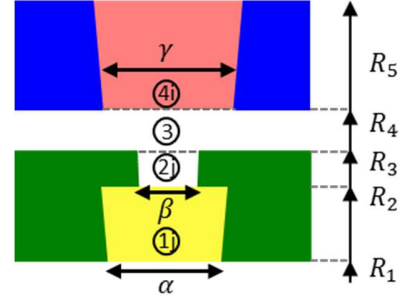


Fig. 2 Division of the airgap in different subdomains

### A. Subdomain Model Overview

The following assumptions are made:

- the problem is 2-D: end effects are neglected;
- stator and rotor iron cores are infinitely permeable;
- geometry is polar;
- input current has a unique frequency  $f_s$ ;
- rotor bars have a uniform electrical conductivity  $\sigma$ ;

The full subdomain model is presented on Fig. 2. It is divided into four types of subdomains:

- $Z_r$  rotor slots (1j),  $j \in \llbracket 1, Z_r \rrbracket$ ,
- $Z_r$  rotor slot openings (2j),
- the air gap (3),
- $Z_s$  stator slot (4i),  $i \in \llbracket 1, Z_s \rrbracket$ .

The magnetic problem is formulated in magnetic vector potential and is solved for each independent time-step. Laplace equation is solved in rotor slot openings (2j) and airgap (3), Poisson equation is solved in stator slots (4i) and Helmholtz equation is solved in rotor bars (1j). At each time step, the current densities in stator slots (4i) and the position of each rotor subdomain are updated. The analytical developments will be explained in details within an upcoming publication.

### B. Airgap Flux Density Results

#### 1) At no load-state

For the no-load simulation, the rotor mechanical speed is set to the synchronous speed at  $N_{rotor} = (1 - s) f_s / p = 1200$  rpm (for  $s = 0$ , where  $s$  is the fundamental slip) so that the fundamental of the rotor current is cancelled. The harmonics of rotor currents due to phase-belt harmonics are neglected as they have a small impact on the magnetic flux density. The time-stepping simulation is performed over a rotor mechanical period  $T_0 = \frac{p}{f_s} = 0.05$  s.

The resulting flux density distribution over space and time results at no-load is shown on Fig. 3 and Fig. 4. Only half of the rotor mechanical period is shown on Fig. 4. At no-load, the radial component is much greater than the tangential one. The highest peak in the flux density FFT is naturally the fundamental of the radial flux density at  $(r, f) = (3, 60 \text{ Hz}) = (p, f_s)$ , where  $r$  is the spatial frequency (also called wavenumber) and  $f$  is the

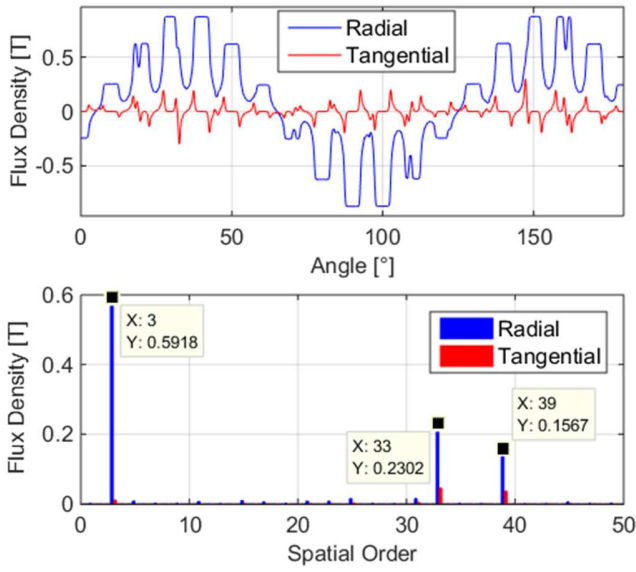


Fig. 3 Airgap flux density distribution over space with FFT at  $s = 0, t = 0.5T_0$

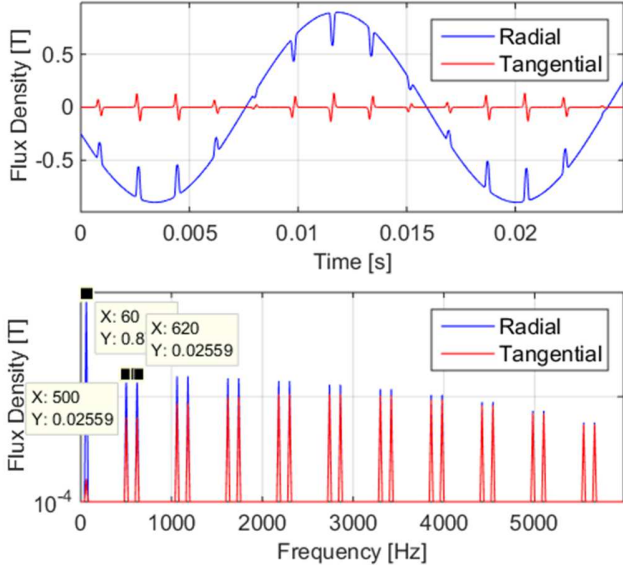


Fig. 4 Airgap flux density distribution over time with FFT at  $s = 0, \theta = \pi$

time frequency. The main spatial harmonics at  $r = \{33; 39\} = Z_s \pm p$  which are due to the stator magnetomotive force (mmf) stepwise distribution and slotting effect. They are present in both radial and tangential components. Spatial harmonics due to rotor slotting at  $r = \{25; 31\} = Z_r \pm p$  have less impact on both flux density components because rotor slots openings are much smaller than stator ones.

Besides, rotor slotting induces harmonics in the flux density time spectrum, named Principal Slotting Harmonics (PSH) (also visible in stator currents) at the following frequencies [15]:

$$f_{psh} = (k \frac{Z_r}{p} (1 - s) \pm 1) f_s; \quad k = 1, 2, 3 \dots \quad (1)$$

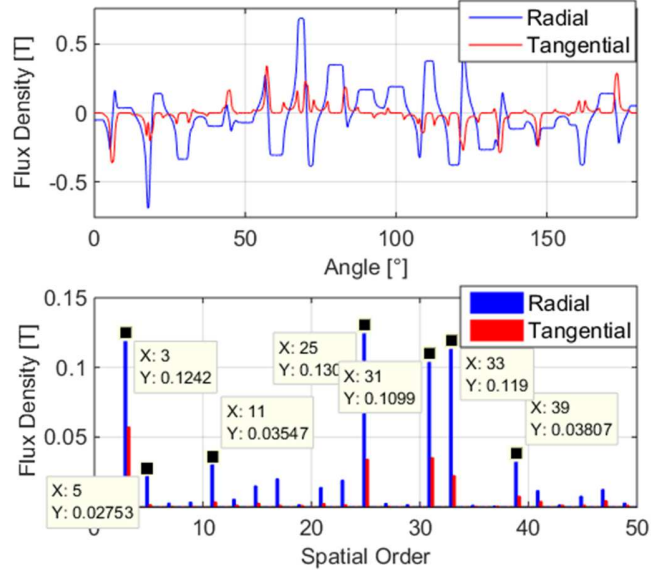


Fig. 5 Airgap flux density distribution over space with FFT at  $s=0.1, t = 0.5T_0$

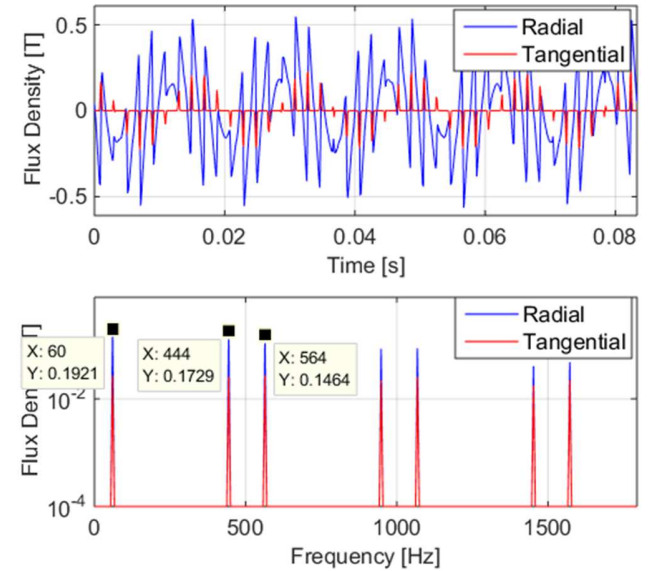


Fig. 6 Airgap flux density distribution over time with FFT at  $slip = 0.1, \theta = \pi$

The first rotor slotting harmonics are for  $k = 1$ , at  $f_{psh1} = \{500 \text{ Hz}; 620 \text{ Hz}\}$  as shown on Fig. 4.

## 2) At load state

For the load simulation, the slip is set at 0.1, meaning that the rotor mechanical speed is now  $N_{rotor} = 1080 \text{ rpm}$ . The simulation is made over a rotor electrical period  $T = 1/(sf_s) = 0.167 \text{ s}$ . The resulting flux density distribution over space and time results is shown on Fig. 5 and Fig. 6. Only half of the rotor electrical period is shown for the time distribution on Fig. 6. As shown on Fig. 5, the fundamental of the radial flux density at  $r = 3 = p$  has considerably decreased contrary to the fundamental of the tangential component (enabling torque production), due to the rotor reaction field. In addition with the

spatial harmonics created by stator mmf and slotting at  $r = \{33; 39\} = Z_s \pm p$ , there are harmonics due to rotor mmf and rotor slotting at  $r = \{25; 31\} = Z_r \pm p$  and those due to the interaction between stator mmf - respectively rotor mmf - and rotor slots - respectively stator slots - at  $r = \{5; 11\} = Z_s - Z_r \pm p$ .

Concerning the time harmonics in the flux density, the first PSH are now at  $f_{psh1} = \{444 \text{ Hz}; 564 \text{ Hz}\}$ , as shown on Fig. 6. Rotor bar currents are induced at the following frequencies in the rotor referential [11]:

$$f_{rm} = (1 - m(1 - s))f_s; \quad m = \pm 6k + 1 \quad (2)$$

The fundamental of the rotor currents is given by  $f_{r0} = sf_s = 6 \text{ Hz}$  (obtained for  $m = 0$  in Eq. (2)) and the first rotor current harmonics are at  $f_{r-5} = 330 \text{ Hz}$  and  $f_{r7} = 318 \text{ Hz}$  in the rotor referential. In the stator referential, the frequency of these two harmonics are in fact the same of the first PSH [16], at  $f_{psh1} = \{444 \text{ Hz}; 564 \text{ Hz}\}$ . The rotor slotting effect and the rotor mmf produce harmonics with the same time frequencies.

### 3) Validation with Ansys Maxwell 2D

The method is fully validated at load state ( $s = 0.1$ ) by transient simulations performed on the finite element software Maxwell 2D [17]. Time step is fixed ( $\Delta t = 0.0001 \text{ s}$ ) and the spatial discretization is 1001 steps per  $180^\circ$ . Only half of the machine is modelled by applying the antisymmetric condition. The mesh on Fig. 7 is automatically generated by Maxwell 2D with the highest density.

Fig. 8 and Fig. 9 show that the SDM model is as accurate as FEA method, while achieving significant time reduction (around 0.1 s per time steps for SDM instead of 20 s for transient FEA). Besides, the transient has to be computed before when using FEA whereas SDM gives directly the steady-state results. The transient represents 23 rotor electrical periods, meaning 3.833 s or 38 333 time steps in the present case. At load state, setting the simulation time to a multiple of the rotor electrical period enables to reduce spectral leakage due to the slip.

### C. Magnetic Forces Computation

#### 1) Maxwell stress tensor

The space and time distribution of the radial and tangential pressures  $\sigma_{rad,tan}$  is computed using the Maxwell stress tensor along a circular path in the air gap:

$$\sigma_{rad}(t, \theta) = \frac{B_{rad}^2(t, \theta) - B_{tan}^2(t, \theta)}{2\mu_0} \quad [N \cdot m^{-2}] \quad (3)$$

$$\sigma_{tan}(t, \theta) = \frac{B_{rad}(t, \theta)B_{tan}(t, \theta)}{\mu_0} \quad [N \cdot m^{-2}] \quad (4)$$

with  $B_{rad}(t, \theta)$  and  $B_{tan}(t, \theta)$  the radial and tangential flux density computed in the previous part. Equation (3) shows that the tangential flux density impacts the radial pressures and is also necessary to determine tangential pressures.

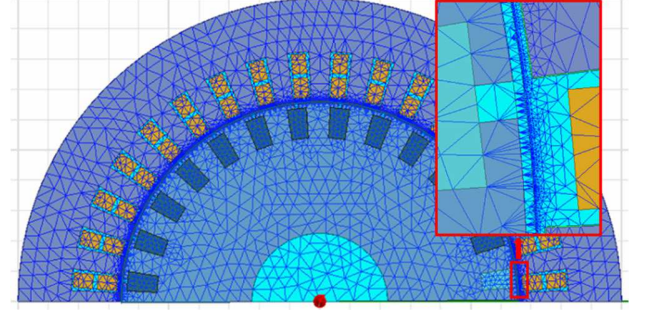


Fig. 7 Maxwell 2D model with mesh plot and zoom in the airgap

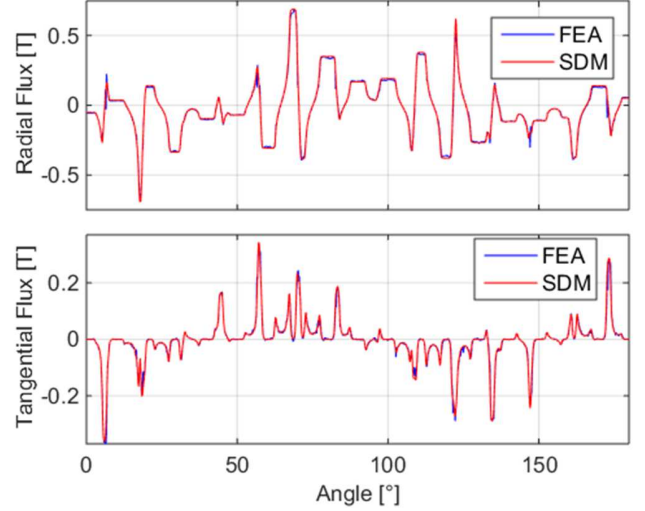


Fig. 8 Airgap flux density comparison over space between FEA (Maxwell software) and SDM (MANATEE software), at  $s = 0.1$ ,  $t = 0.5T_0$

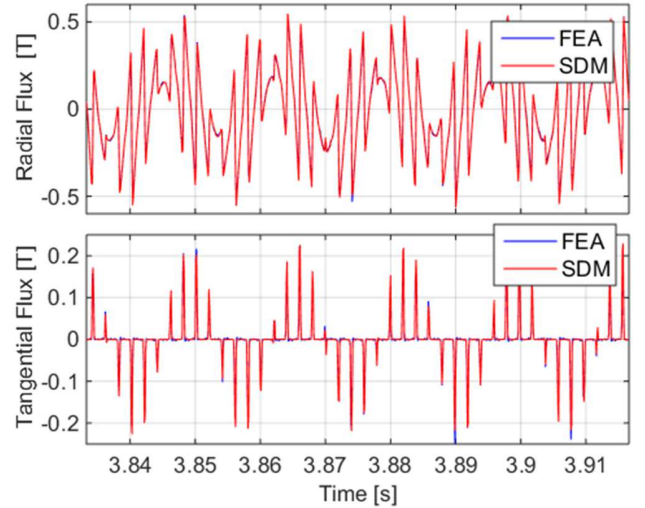


Fig. 9 Airgap flux density comparison over time between FEA (Maxwell software) and SDM (MANATEE software at  $s = 0.1$ ,  $t = 0.5T_0$

With this computation method, it is easy to keep or remove tangential effects. Forces are deduced from pressures by integrating over the application surface.

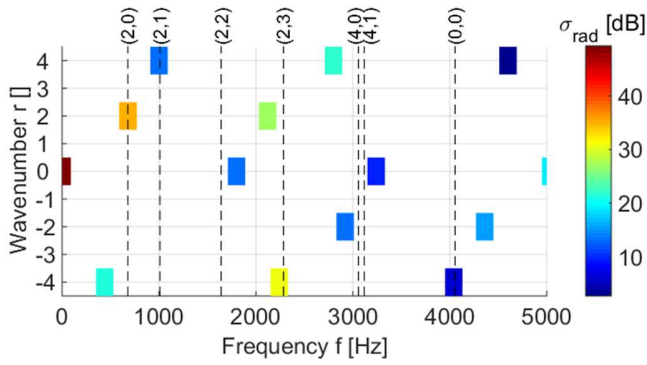


Fig. 10 Radial pressure  $\sigma_{rad}$  FFT2D at no-load and synchronous speed  $N = 1200$  RPM. Structural modes are represented in vertical dotted lines. A resonance may occur between the excitation and the radial mode (2,0) at 678Hz.

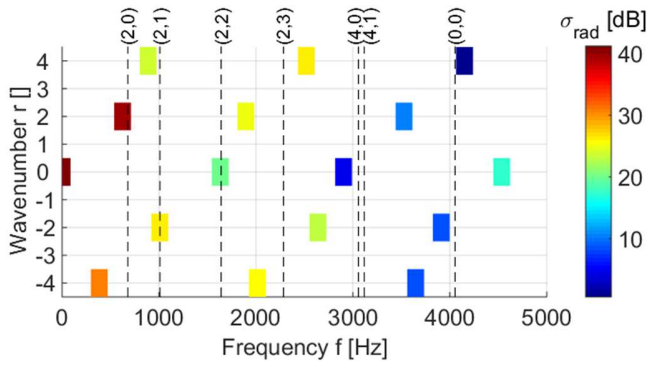


Fig. 11 Radial pressure  $\sigma_{rad}$  FFT2D at load and asynchronous speed  $N = 1080$  RPM. The same couples  $(f, r)$  can be observed as at no-load state.

## 2) Harmonic formulation (2D Fourier Transform)

Harmonics of pressure are obtained by performing a 2D Fourier Transform of the space and time pressure distribution:

$$\sigma_{rad,tan}(t, \theta) = \sum_{f,r} \sigma_{fr} e^{j(2\pi ft - r\theta + \varphi_{fr})} \quad (5)$$

where:

- $(f, r)$  is the couple of frequency and wavenumber for each pressure harmonic;
- $\sigma_{fr}$  is the magnitude of the harmonic  $(f, r)$ ;
- $\varphi_{fr}$  is the phase of the harmonic  $(f, r)$ ;

Radial pressure FFT2D is shown on Fig. 10 and Fig. 11 for both no-load and load cases. Radial and tangential pressures have the same harmonic content, meaning that the same couples  $(f, r)$  are non-nul in both FFT2D. Pressure harmonics of low wavenumbers are likely to excite structural modes and generate a high level of vibrations and potentially noise in the audible frequencies. The least non null wavenumber  $r_{min}$  is given by the following rule (for induction machine with distributed windings):

$$r_{min} = GCD(Z_s, Z_r, 2p) = 2 \quad (6)$$

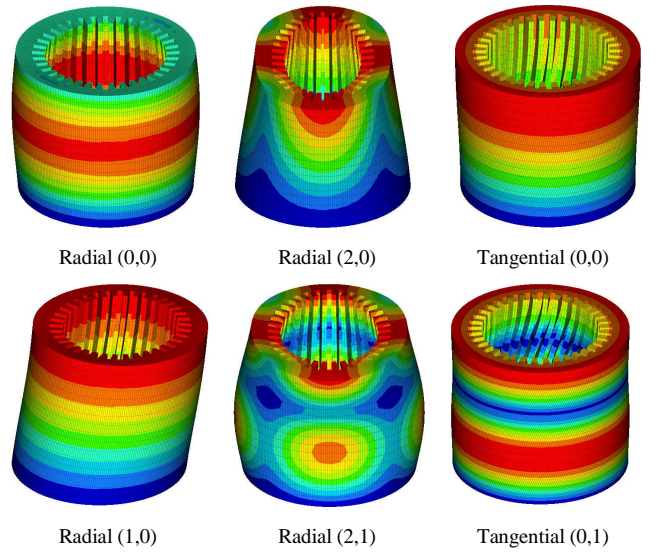


Fig. 12 Illustrations of radial and tangential modes  $(m,n)$

The least frequency for which  $r_{min}$  is reached is  $f_{min,2} = (Z_r/p(1-s) + 2)f_s = 680$  Hz at no-load with  $r_{min} = Z_s - Z_r - 2p = 2$ . This results from the combination of the first stator slotting modulation of the fundamental flux density at  $(f_s, Z_s - p)$  with the first rotor slotting modulation of the fundamental flux density  $((Z_r/p(1-s) + 1)f_s, -Z_r - p)$ . This slotting excitation in particular may resonate with the mode (2,0) at variable speed for both no-load and load cases.

## IV. ELECTROMAGNETIC VIBRATION SYNTHESIS (EVS)

### A. Principle

The direct calculation of the vibrations due to magnetic forces requires high computing time, especially at variable speed. Variable speed operation only changes the magnitude of magnetic forces, but their wavenumbers remain the same. Besides that, the mechanical response of the stator can be considered as linear. It is therefore possible to characterize the vibration behavior of the stator under some unit magnitude rotating force waves, giving some Frequency Response Functions (FRF) accounting for the structural modes (see for instance [7]). The FRF are here computed by using the automated coupling between MANATEE and the numerical software Hypermesh/Optistruct. As shown in [18], the coupling consists in automatically generating both CAD and mesh of the stator in Hypermesh, so that the user can directly run the solver Optistruct, re-import the results in MANATEE, perform Electromagnetic Vibration Synthesis and finally calculate emitted acoustic noise using MANATEE built-in semi analytical acoustic models.

### B. Stator modal analysis

The natural frequencies associated to each structural mode are given in TABLE II. Each mode is classically characterized by the direction of the deflection – either radial or tangential – and the couple  $(m, n)$  where  $m$  is the circumferential order and  $n$  is the axial order of the deflection. Only the radial modes with “low” circumferential orders  $m$  will generally have an influence

TABLE II. STRUCTURAL MODES

Radial (yoke deflection)		Tangential (pure tooth bending)	
Mode(m,n)	Frequency [Hz]	Mode(m,n)	Frequency [Hz]
(0,0)	4054	(0,0)	338
(1,0)	278	(0,1)	1015
(2,0)	678	(0,2)	1695
(2,1)	1009	(0,3)	2372
(2,2)	1641	(0,4)	3037
(2,3)	1641		
(3,0)	1718		
(3,1)	1850		
(4,0)	3057		
(4,1)	3118		

TABLE III. ELASTIC PROPERTIES OF LAMINATION M400-50A

Young modulus [MPa]		Shear modulus [MPa]		Poisson ratio	
$E_x$	215	$G_{xy}$	82.7	$\nu_{xy}$	0.3
$E_y$	215	$G_{yz}$	2	$\nu_{yz}$	0.03
$E_z$	80	$G_{zx}$	2	$\nu_{zx}$	0.03

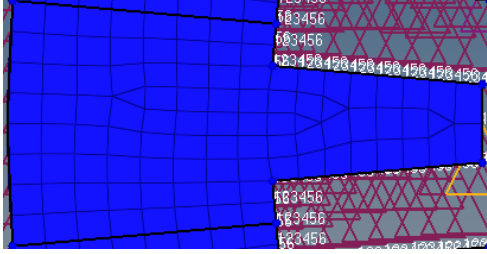
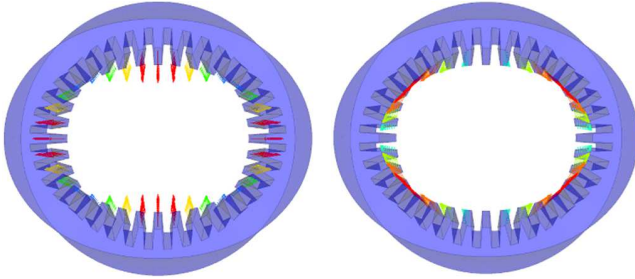


Fig. 13 Tooth meshing in Optistruct for modal analysis and FRF computation

Fig. 14 Unit force wave at  $r = 2$  inducing a radial deflection of  $r = 2$ 

of noise and vibrations [1], especially the modes  $\{(0,0), (2,0), (2,1)\}$  shown on Fig. 12. Tangential modes involving pure tooth bending modes generally induce radial vibrations of lower magnitude.

For model simplicity, the stator is considered without frame and winding, with clamped-free boundary conditions. The tooth meshing is shown on Fig. 13 and is duplicated for each tooth. The number of axial layer is 16 to enable to catch longitudinal modes. The stator lamination is M400-50A for which the density is  $7650 \text{ kg/m}^3$  and the orthotropic elastic properties are listed in TABLE III.

### C. Frequency Response Function (FRF)

Unit rotating wave of pressure  $(f, r)$  are successively injected at the tip of stator teeth, first in the radial direction and secondly in the tangential one, with  $r \in \{-4, -2, 0, 2, 4\}$  and

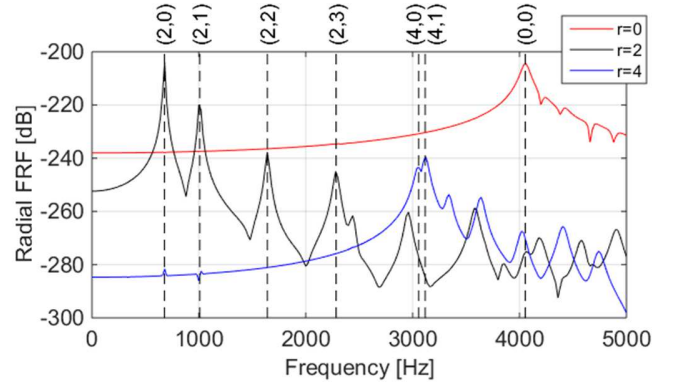


Fig. 15 Radial FRF for the stator external yoke displacement

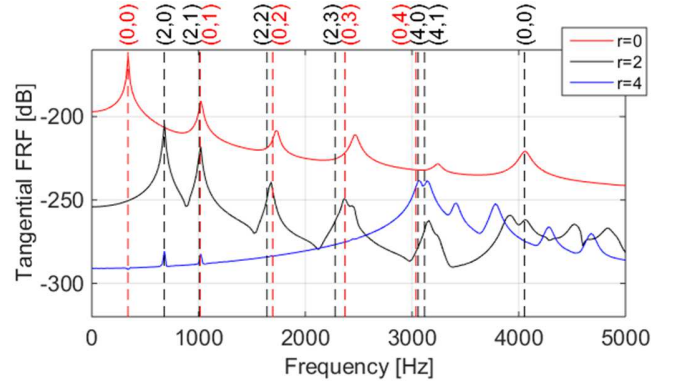


Fig. 16 Tangential FRF for the stator external yoke displacement

$f \in \{0:20\text{Hz}:5000 \text{ Hz}\}$ . Negative wavenumbers account for different rotating force wave directions in order to model pulsating force waves that can be present in magnetic excitations, especially in case of non-sinusoidal supply. The applied force is uniform along the axial direction.

The resulting FRF are shown on Fig. 15 and Fig. 16. They represent the radial displacement of the stator yoke per pressure unit expressed in  $\text{dB}$ . The radial – respectively tangential – structural modes are represented in black – respectively red – dotted vertical lines. One can see that both radial and tangential waves can generate a radial deflection and so potentially excite the radial structural modes, contrary to what is generally assumed. Fig. 15 confirms the resonance effect between magnetic excitation and structural modes [21]. It means that the displacement level is strongly amplified when the excitation wavenumber  $r$  is the same as the mode circumferential order  $m$  (independently of the axial order  $n$ ) and the excitation frequency  $f$  is close to the natural frequency  $f_m$  of the mode, meaning:

$$\begin{cases} r = m \\ f \approx f_m \end{cases} \quad (7)$$

Besides, the greater is the axial order  $n$ , the lower is the resonance peak. Concerning the tangential FRF on Fig. 16, one can see that tangential excitations of wavenumber  $r = 0$  excite the tangential modes  $(0, n)$  while tangential excitations with  $r = \{2, 4\}$  resonate with the radial modes of same order, giving the same FRF as for radial excitations. However, tangential excitations magnitudes are smaller than radial ones, hence the

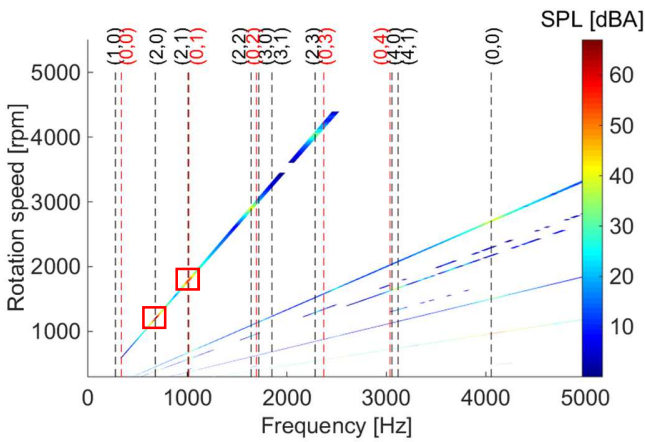


Fig. 17 A-weighted sound pressure level sonagram at 1 meter and at no-load

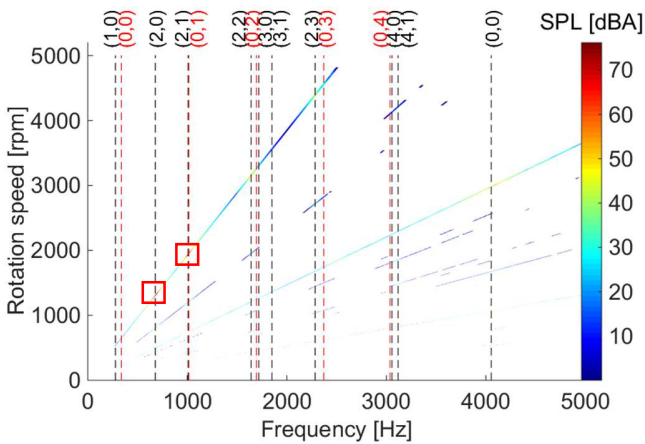


Fig. 18 A-weighted sound pressure level sonagram at 1 meter and at load

contribution of the tangential forces can only be quantified with the Electromagnetic Vibration Synthesis of all the exciting harmonics [18].

#### D. Electromagnetic Vibration Synthesis and Emitted Noise

Radial and tangential pressures which were computed is the previous part at no-load and load state at their respective operating speed are extrapolated over the variable speed range  $N = \{0: 20\text{Hz}: 5000\text{ Hz}\}$ . This way, input stator phase current and slip are kept constant and only the supply frequency increases. Naturally, an error is made on the flux density computation at load case because the rotor mmf changes due to skin effect. However, this enables to keep the magnetic forces constant in function of speed and see only the tangential effects on the variable speed sonogram, which represents the Sound Pressure Level (SPL) spectrum as a function of the rotating speed. The Electromagnetic Vibration Synthesis is performed in MANATEE software by summing all the contributions of the harmonics of radial and tangential excitations multiplied by the FRF. The sound pressure level emitted by the stator is obtained by using the semi-analytical radiation factor of an equivalent cylinder [19].

The sonograms are shown in Fig. 17 and Fig. 18 at respectively no-load and load cases. On both sonograms, two main resonances can be identified at (680 Hz, 1200 RPM) and

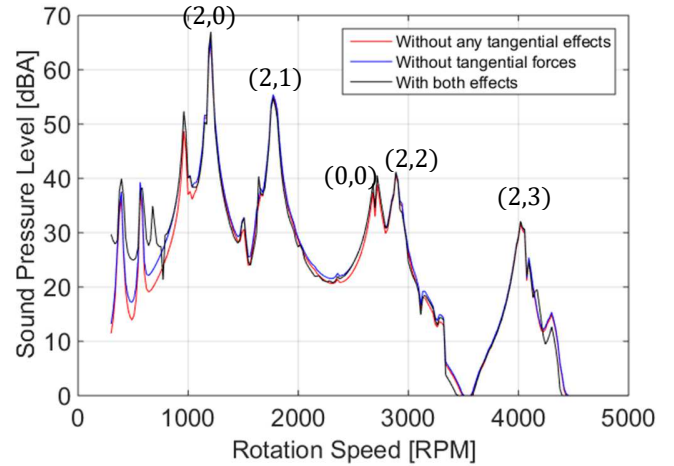


Fig. 19 Comparison of the overall SPL [dBA] at no-load in function of rotation speed including all, only one or none tangential effects

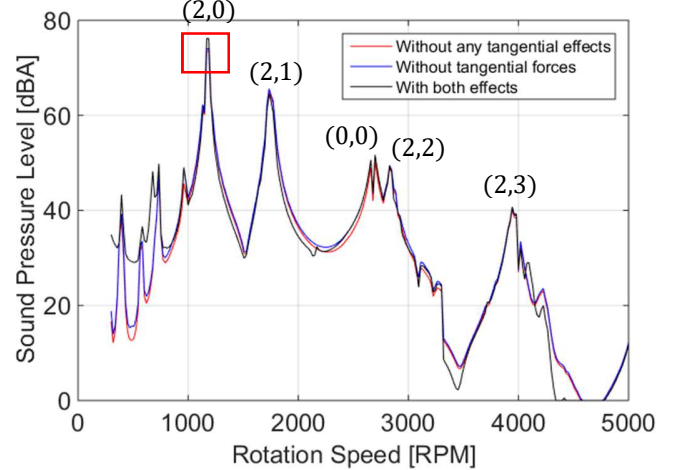


Fig. 20 Comparison of the overall SPL [dBA] at load in function of rotation speed including all, only one or none tangential effects

(1010 Hz, 1800 RPM) due to the first slotting harmonic (identified in III.C.2) which successively excites the radial modes (2,0) and (2,1). This harmonic excites every radial mode (2,  $n$ ). A small resonance with the radial “breathing” mode (0,0) can be observed at (4000 Hz, 2700 RPM).

#### E. Tangential effects on overall SPL

The sound pressure level is also computed only with the effect of the tangential flux density on the radial forces (excluding tangential forces in the FRF) and without any tangential effects. The three resulting overall SPL in function of the rotation speed are compared on Fig. 19 and Fig. 20 at no-load and load cases. At the largest resonance peak and at load state, the SPL is +2 dBA more by including both tangential effects and +0.3 dBA by only including the effect of the tangential flux density on the radial force. At no-load, the maximum difference is less than 1.5 dB.

This small difference is probably due to the fact that the stator yoke is quite thick compared with the stator tooth length. A thinner yoke would increase the impact of the tangential FRF on the radial vibrations. The orthotropic elastic properties may

have also an influence on the tangential FRF, especially if different boundary conditions of the stator are applied. Finally, the tangential field effects could be quantified using this method for electric machines with larger magnetic airgap such as surface permanent magnet synchronous machines.

## V. CONCLUSION

In this paper, noise and vibrations due to magnetic forces in an induction machine with 3 pole pairs for traction application have been studied regarding the effect of the tangential flux density on the radial forces and the effect of the tangential forces on radial vibrations. A fast subdomain model has been developed for induction machines and validated with finite elements to quickly calculate the airgap Maxwell stress distribution, and the Electromagnetic Vibration Synthesis method has been applied within MANATEE simulation environment. As expected, these two “tangential effects” have a rather small impact on the resulting noise level: in the case of this particular machine, a maximum error of 2 dB is made if both tangential effects are neglected as it is done in vibroacoustic studies of electrical machines. Tangential effects may have a greater impact when considering a smaller stator yoke thickness to tooth length ratio and the methodology should be extended to high pole pair number machines and permanent magnet synchronous machines.

## REFERENCES

- [1] J. Le Besnerais, “Fast Prediction of Variable-Speed Acoustic Noise and Vibrations due to Magnetic Forces in Electrical Machines,” in *ICEM International Conference on Electrical Machines*, 2016.
- [2] M. Hecquet, A. Ait-Hammouda, M. Goueygou, P. Brochet, and A. Randria, “Prediction of the electromagnetic noise of an asynchronous machine using experimental designs,” *Math. Comput. Simul.*, vol. 71, no. 4–6, pp. 499–509, Jun. 2006.
- [3] Z. Q. Zhu, Z. P. Xia, L. J. Wu, and G. W. Jewell, “Analytical modeling and finite-element computation of radial vibration force in fractional-slot permanent-magnet brushless machines,” *IEEE Trans. Ind. Appl.*, vol. 46, no. 5, pp. 1908–1918, 2010.
- [4] M. Valavi, A. Nysveen, R. Nilssen, R. D. Lorenz, and T. Rølvåg, “Influence of pole and slot combinations on magnetic forces and vibration in low-speed PM wind generators,” *IEEE Trans. Magn.*, vol. 50, no. 5, pp. 1–11, 2014.
- [5] F. Qi and X. Wang, “Tangential force effect on the vibration and noise of PMDC motor,” in *2013 5th International Conference on Power Electronics Systems and Applications, PESA 2013*, 2013, pp. 2–6.
- [6] S. D. Garvey and G. D. Le Flem, “Tangential Forces Matter,” in *Ninth International Conference on Electrical Machines and Drives*, 1999, no. 468, pp. 174–178.
- [7] J. Roivainen, “Unit-wave response-based modeling of electromechanical noise and vibration of electrical machines,” Helsinki University of Technology, 2009.
- [8] E. Devillers, J. Le Besnerais, T. Lubin, M. Hecquet, and J. P. Leconte, “A review of subdomain modeling techniques in electrical machines: performances and applications,” in *ICEM International Conference on Electrical Machines*, 2016.
- [9] L. J. Wu, Z. Q. Zhu, J. T. Chen, and Z. P. Xia, “An Analytical Model of Unbalanced Magnetic Force in Fractional-Slot Surface-Mounted Permanent Magnet Machines,” *IEEE Trans. Magn.*, vol. 46, no. 7, pp. 2686–2700, Jul. 2010.
- [10] J. Boisson, F. Louf, J. Ojeda, X. Mininger, and M. Gabsi, “Analytical approach for magnetic and acoustic modeling of flux-switching permanent-magnet motors: Application to geometrical optimization,” *2014 17th Int. Conf. Electr. Mach. Syst. ICEMS 2014*, vol. 3, no. Section II, pp. 3060–3066, 2015.
- [11] T. Lubin, S. Mezani, and A. Rezzoug, “Analytic Calculation of Eddy Currents in the Slots of Electrical Machines: Application to Cage Rotor Induction Motors,” *IEEE Trans. Magn.*, vol. 47, no. 11, pp. 4650–4659, 2011.
- [12] K. Boughrara, N. Takorabet, R. Ibtouen, O. Touhami, and F. Dubas, “Analytical Analysis of Cage Rotor Induction Motors in Healthy, Defective and Broken Bars Conditions,” *IEEE Trans. Magn.*, vol. 2, no. c, pp. 1–1, 2014.
- [13] R. L. J. Sprangers, J. J. H. Paulides, B. L. J. Gysen, E. a. Lomonova, and J. Waarma, “Electric circuit coupling of a slotted semi-analytical model for induction motors based on harmonic modeling,” *2014 IEEE Energy Convers. Congr. Expo.*, pp. 1301–1308, 2014.
- [14] Eomys Engineering, “MANATEE,” 2016. [Online]. Available: <http://eomys.com/produits/manatee>.
- [15] S. Nandi, “Modeling of induction machines including stator and rotor slot effects,” *IEEE Trans. Ind. Appl.*, vol. 40, no. 4, pp. 1058–1065, 2004.
- [16] M. G. Joksimovic, M. Djurovic, and J. Penman, “Cage rotor MMF: winding function approach,” *IEEE Power Eng. Rev.*, vol. 21, no. 4, pp. 64–66, 2001.
- [17] Ansys, “Maxwell 2D v16,” 2016. [Online]. Available: <http://www.ansys.com/products/electronics/ansys-maxwell>.
- [18] M. Régniez, Q. Souron, P. Bonneel, and J. Le Besnerais, “Numerical simulation of structural-borne vibrations due to electromagnetic forces in electric machines – coupling between Altair Optistruct and Manatee software,” *Researchgate*.
- [19] J. F. Gieras, C. Wang, and J. C. Lai, *Noise of polyphase electric motors*. 2006.
- [20] J. Le Besnerais, “Reduction of magnetic noise in PWM-supplied induction machines - low-noise design rules and multi-objective optimization,” PhD Thesis, Ecole Centrale de Lille, 2008.